JOURNAL OF GEOPHYSICAL RESEARCH, VOL. 102, NO. C11, PAGES 24,987–25,003, NOVEMBER 15, 1997

Subtidal circulation on the Scotian Shelf: Assessing the hindcast skill of a linear, barotropic model

Keith R. Thompson and Jinyu Sheng

Department of Oceanography, Dalhousie University, Halifax, Nova Scotia, Canada

Abstract. Currents measured during the winter of 1985-1986 by four moorings on the inner Scotian Shelf are used to assess the hindcast skill of a three–dimensional circulation model forced by local wind stress and coastal sea level. The model is linear and barotropic. The integration scheme is based on the modification of the Galerkin spectral method proposed recently by *Sheng and Thompson* [1993]. The skill of the model is measured by the variance of the hindcast errors divided by the variance of the observations (henceforth γ^2). The model is most effective within 30 km of shore ($0.51 \leq \gamma^2 \leq 0.66$). At the mooring in the Nova Scotia Current, a surface intensified southwestward jet with its center approximately 50 km from shore, the model fails to capture the bulk of the variance at current meters within 70 m of the surface ($0.81 \leq \gamma^2 \leq 0.87$). The skill of the model is lowest at the mooring 65 km from shore ($0.92 \leq \gamma^2 \leq 0.94$). To put these measures of skill into perspective, the currents are hindcast using a linear statistical model with the same inputs as the circulation model. The statistical model is optimal in the sense no other linear model with these inputs can achieve a lower hindcast error variance. For half of the current meters within 30 km of shore and two in the Nova Scotia Current the skill of the circulation model is not significantly lower than that of the statistical model. The largest discrepancies in the skill of the two models are found at the offshore mooring. We show that the suboptimal performance of the circulation model is due in part to the assumption of a spatially uniform wind field. We speculate that another contributing factor is the assumed form of the sea level profile along the open boundary that is upstream in the sense of coastal trapped wave propagation. Finally, the statistical model is used to estimate the increase in skill of the circulation model that may result from the assimilation of hydrographic data and additional coastal sea levels.

1. Introduction

There is growing interest in operational modeling of shelf circulation. Applications include the forecasting of oil spill and iceberg trajectories, the design and operation of offshore structures, and marine search and rescue. We are working toward an operational model of the circulation over the continental shelf of eastern Canada. In its complete form the model will assimilate coastal sea level and other readily available data. As a step in the development of such a model, we present here an assessment of the skill of a linear dynamical model forced by local wind stress and sea level from a single coastal tide gauge. A statistical model is used to estimate the extent to which the circulation model can be improved by tuning, for example, friction coefficients and assimilating sea level from more coastal sites. We recognize that some circulation patterns are not driven by wind and have no signature in coastal sea level. Another objective of the present study is to map out these patterns and quantify their contribution to the observed circulation variability on the Scotian Shelf.

Paper number 97JC00368.
0148-0227/97/97JC-00368$09.00

The circulation model is based on a modification of the Galerkin spectral technique proposed by *Sheng and Thompson* [1993, henceforth ST93]. The modification involves the subtraction of a steady Ekman solution from the flow at each grid point before expanding the vertical structure in terms of eddy viscosity eigenfunctions. The rationale is to remove most of the wind-driven shear and thereby reduce the number of eigenfunctions required to describe the vertical structure of the flow. In a series of calculations using idealized bathymetry and time-harmonic wind forcing, ST93 showed that accurate flow fields could be obtained with only 4 eigenfunctions. In this study we show that a similar number of eigenfunctions will suffice with realistic winds and bathymetry.

The location chosen to test the circulation model is the Scotian Shelf. The bathymetry is typical of the eastern seaboard of Canada with a chain of offshore banks and deep basins inshore (Figure 1). The mean surface flow is about 10 cm s^{-1} to the southwest. It is part of a large-scale baroclinic flow that connects the Labrador Shelf, Gulf of St. Lawrence, Gulf of Maine, and Mid-Atlantic Bight [e.g.,

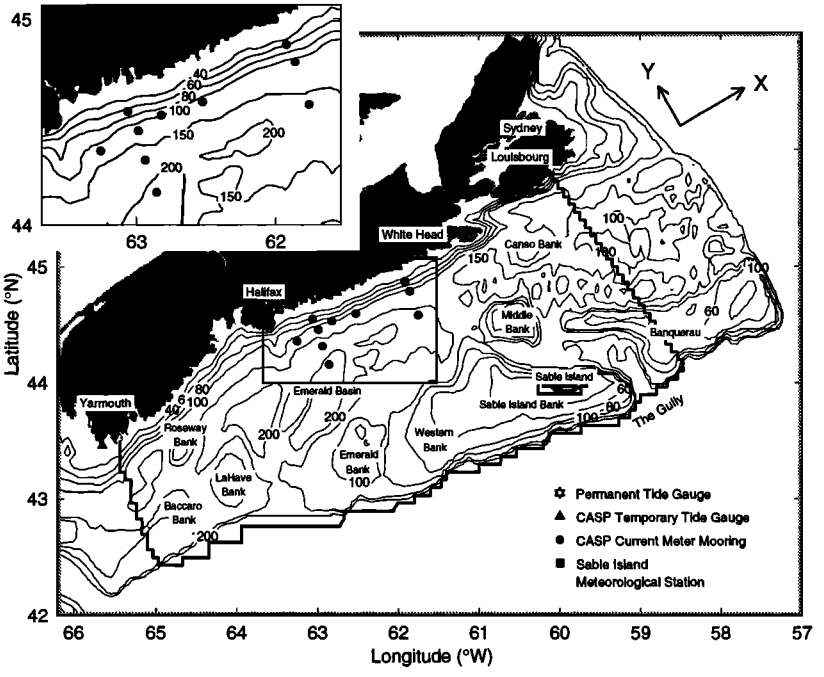

Figure 1. Scotian Shelf bathymetry and the Canadian Atlantic Storms Program (CASP) instrument array. The Halifax Line is defined by the line of four moorings running from the coast to Emerald Basin. The open boundaries of the circulation model are shown by the thick lines. The cross-shelf boundary to the west is the "forward" boundary, and the cross-shelf boundary to the east is the "backward" boundary. The "offshore" boundary runs along the shelf break. The alongshore components of current (u) and wind stress (τ_x) are positive toward 68°T. The onshore components of current (v) and wind stress (τ_y) are positive toward 338°T.

Smith and Schwing, 1991, and references therein]. The data used to drive and validate the model were collected in the winter of 1985-1986 during the Canadian Atlantic Storms Program (CASP). Analyses of this extensive set of current, coastal sea level, bottom pressure, surface wave, and hydrographic data have identified buoyancy input, local wind stress, and remotely-generated coastal trapped waves as important drivers of the subtidal circulation [*Schwing*, 1989, 1992a, b; *Smith and Schwing*, 1991].

It is well known that continental shelves can act as guides for coastal trapped waves [e.g., *LeBlond and Mysak*, 1978]. It follows that open boundaries of shelf circulation models that are upstream in the sense of wave propagation (the so-called "backward" boundaries) are potentially important sources of energy. The specification of the backward boundary condition is a difficult problem for limited-area modelers that has resulted in some ad hoc solutions. For example, in a study of circulation in the Gulf of Maine, *Wright et al.* [1987] assumed a linear drop in sea level along their backward boundary that was proportional to the along shelf wind stress. In this way they hoped to account for the effect of wind stresses acting over regions not included in their model. In a study of time-varying circulation on the Scotian Shelf, *Schwing* [1992b] forced a linear barotropic model with a variable amplitude, first-mode shelf wave at the backward boundary. In this way Schwing was able to reproduce some of the empirical relationships found in his earlier statistical studies [*Schwing*, 1989, 1992a] and thereby provide the most convincing evidence to date for the existence of shelf waves in this region.

In the present study we use the ST93 model to hindcast currents observed on the Scotian Shelf during CASP. The model is forced by wind stress, and its backward boundary condition is specified using observed coastal sea level. There are two major differences between the ST93 model and that used by *Schwing* [1992b]. The ST93 model is three dimensional, in contrast to the depth-averaged model of Schwing. The ST93 model can therefore accommodate a more realistic parameterization of bottom stress in terms of bottom velocity. The second major difference is that the ST93 model is time stepping in contrast to the time harmonic model of Schwing. Although time–harmonic models are computationally efficient and have proved useful in understanding the dynamical response of shelf seas to local and remote forcing, it is difficult to envision how they might be used operationally to nowcast and forecast shelf circulation.

We quantify the performance of the ST93 model by comparing its hindcasts against an independent set of current measurements made during CASP. The skill of the model is measured by the variance of the hindcast errors divided by the variance of the observations (henceforth denoted by γ^2). In general, the smaller the γ^2, the higher the skill of the model. If γ^2 is less than unity, the observed variance is reduced by subtracting the hindcasts from the observed currents.

We will show, for example, that γ^2 is 0.5 at the mooring 30 km from shore. Can the circulation model be adjusted in some way to reduce this value of γ^2? To answer this question, we hindcast the currents with a linear statistical model that has the same inputs as the circulation model. The statis-

tical model is optimal in the sense that no other linear model, dynamical or otherwise, can achieve a lower γ^2. We are thus able to show, for example, that the circulation model is close to optimal at the mooring 30 km from shore. Differences in the frequency-dependent responses of the circulation and statistical models are useful in diagnosing the cause of the hindcast errors of the circulation model. For example, such differences lead us to conclude that the wind field over the Scotian Shelf cannot be treated as spatially uniform and to speculate that the form of the backward boundary condition should change with frequency.

In section 2 we describe the CASP experiment and summarize the subtidal current variability. In section 3 we outline the ST93 model and determine the number of eigenfunctions required to hindcast the CASP observations. In section 4 we examine the steady response of the model to wind forcing and flows through its open boundaries. The time-varying response of the model is compared against observations in section 5. Ways of improving the hindcasts are discussed in section 6. Results are discussed, and suggestions are made for future work in section 7.

2. Description of Current Variability

The CASP instrument array consisted of two lines of moorings running across the Scotian Shelf and one line running along the 100 m isobath (Figures 1 and 2). In this study we focus on currents measured by the four moorings on the Halifax Line (Figure 2). Mooring 1 and 2 were within 30 km of shore and will be referred to as the nearshore moorings. Mooring 3 was about 45 km from shore and lay in the path of the Nova Scotia Current, a primarily baroclinic coastal jet that flows along the shelf to the southwest. Mooring 4 was about 65 km from shore and will be referred to as the offshore mooring. Coastal sea level was recorded by three permanent tide gauges and bottom pressure was recorded by seven temporary coastal gauges (see Figure 1). Wind speed and direction were recorded at Sable Island and five mainland stations. *Lively* [1988] provides a complete data inventory and details of the data processing. *Anderson and Smith* [1989] give the rationale for the CASP experiment and some statistics summarizing the observed currents and hydrography. More extensive analyses are given by *Schwing* [1989, 1992a, b] and Smith and Schwing [1991].

The coastal sea levels were isostatically adjusted to remove the effect of air pressure (specifically, η was replaced by $\eta + p_a/g\rho_0$, where ρ_0 is a reference water density and p_a is air pressure). Bottom pressure was converted into adjusted sea level through division by $g\rho_0$. We will henceforth refer to adjusted sea level as sea level. Currents and sea levels were low-pass filtered to eliminate diurnal and semidiurnal tides. The filter had a cutoff period of 27 hours. Wind was transformed into stress using the parameterization of *Large and Pond* [1981] and then low-pass filtered. Time series of Louisbourg sea level and Sable wind stress, the inputs to the circulation and statistical models, are plotted in Figure 3. Typical nearshore current time series and their power and coherency spectra are shown in Figure 3 and Figure 4, respectively.

Observed Currents

Mean flow on the Halifax Line is dominated by a surface-intensified, alongshore jet centered on mooring 3. The flow at this mooring is to the southwest with a maximum speed of about 30 cm s^{-1} [*Anderson and Smith*, 1989]. Flow at the adjacent moorings is also to the southwest but at about 10 cm s^{-1}. The mean flow at mooring 1 is less than 3 cm s^{-1}.

Current variance ($s_u^2 + s_v^2$) has been split into two parts: one is associated with motions along the major principal axis

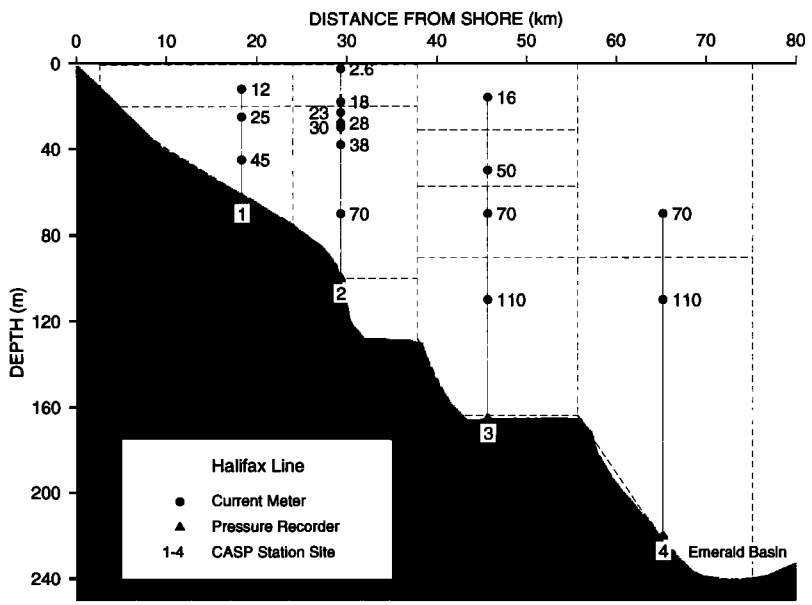

Figure 2. Halifax Line observing array. The latitudes and longitudes of moorings 1 through 4 are shown in Figure 1. The cross-sectional areas defined by the dashed lines are used to calculate alongshore transport as described in the text.

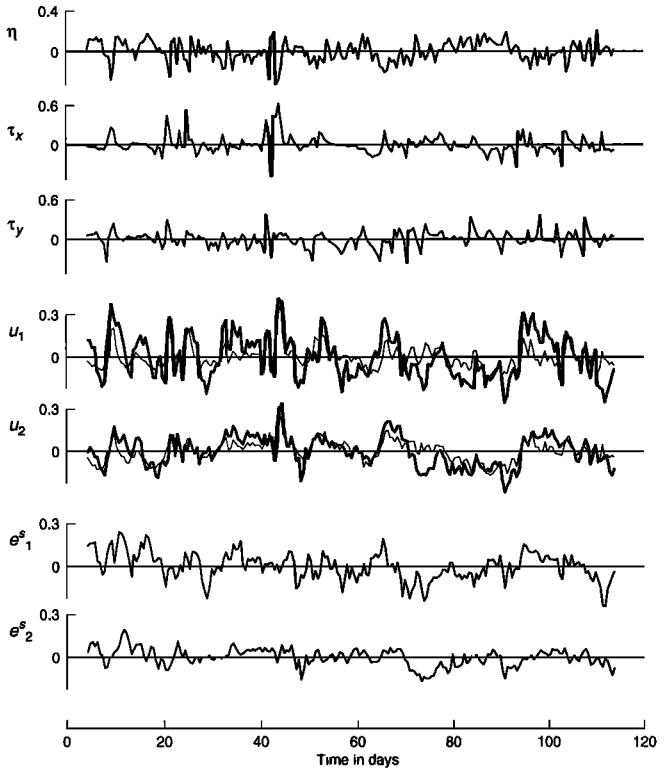

Figure 3. Typical time series. From top to bottom: η, Louisbourg sea level in meters; τ_x and τ_y, alongshore and onshore components of wind stress at Sable Island in pascals; u_1, observed alongshore flow at 25 m on mooring 1 (thick line), and hindcasts (thin line) from the circulation model, both in meters per second ; u_2, as for u_1, but at 23 m on mooring 2; e_1^s, residuals from the statistical model (see (3)) at 25 m on mooring 1 in meters per second; e_2^s, as for e_1^s, but at 23 m on mooring 2. The start time is 2200 UT November 28, 1985, and the sampling interval is 12 hours.

of variation (s_p^2) and the other part is associated with motions orthogonal to this axis ($s_u^2 + s_v^2 - s_p^2$). If the motion is isotropic, the ratio $s_p^2/(s_u^2 + s_v^2)$ equals one half; if the motion is rectilinear, the ratio equals unity. The orientation of the major principal axis is denoted by θ, and we measure it clockwise with respect to the nominal alongshore direction of 68°T.

In Table 1 we list $s_u^2 + s_v^2$, $s_p^2/(s_u^2 + s_v^2)$, and θ for the 13 current meters on the Halifax Line. Broadly speaking, current variance decreases with distance from shore. For example, the variance at the offshore mooring is about one third of the variance at mooring 1. The mooring in the Nova Scotia Current is an exception. At this location the current variance increases with distance off the seabed. In fact, the near-surface flow at mooring 3 is about as energetic as the flow at mooring 1. At the nearshore moorings the flow is primarily alongshore ($s_p^2/(s_u^2 + s_v^2) \approx 0.9$, $|\theta| < 23°$). In the Nova Scotia Current the principal axes are also oriented approximately alongshore ($|\theta| < 14°$), but there is a tendency for motion to become increasingly isotropic with distance from the seabed. At the offshore mooring the principal axes are rotated counter-clockwise by about 30° with respect to the nominal alongshore direction of 68°T. This is probably due to the fact that the depth contours run closer to 40°T at this mooring (Figure 1).

The dominant spatial patterns of current variation on the Halifax Line were determined by principal component analysis. (The analysis was based on the 26 × 26 covariance matrix of u and v components measured by the 13 current meters.) The first mode of variation, $\vec{\phi}_1$, accounts for 51% of the current variance (Figure 5a). This mode can be interpreted as a depth-independent, coastally intensified jet. Its time-varying amplitude, α_1, has a standard deviation of 32 cm s^{-1}. The elements of $\vec{\phi}_1$ associated with the nearshore meters are about 0.3 in magnitude, and so the nearshore currents attributable to this mode of variation have a standard deviation of about $0.3 \times 32 = 9.6$ cm s^{-1}. The second mode of variation, $\vec{\phi}_2$, accounts for an additional 14% of the variance (Figure 6a). It can be interpreted as a surface-intensified, alongshore jet centered on mooring 3. The time variation of its amplitude, α_2, is dominated by a linear trend that translates into a gradual weakening of the Nova Scotian Current by about 25 cm s^{-1} over the CASP period.

To provide a preliminary physical interpretation of the first mode of variation, we regressed α_1 on the wind. We found a statistically significant correlation ($r^2 = 0.34$) between the alongshore component of Yarmouth wind stress and α_1 lagged by 12 hours. This suggests that the first mode of variation is driven in part by local wind. We also checked if changes in α_1 could be detected in coastal sea level. We regressed sea level measured at the shoreward end of the mooring line on α_1 and found the fit was optimal at zero lag ($r^2 = 0.55$). The regression coefficient implied a 26 cm drop in coastal sea level for each 1 m s^{-1} increase in α_1. Is such a drop consistent with simple geostrophic balance? Let $\Delta\eta$ denote the drop in sea level along the Halifax Line from its seaward end to the coast. If $\vec{\phi}_1$ is in geostrophic balance, an increase in α_1 of 1 m s^{-1} should be associated with an increase in $\Delta\eta$ of 17 cm. (We estimated $\Delta\eta$ by $-fg^{-1}\sum_i u_i \Delta y_i$, where the u_i are elements of $\vec{\phi}_1$ associated with the top meters on moorings 1 through 4 and Δy_i are the corresponding widths of the cross-sectional areas defined in Figure 2.) Thus most of the 26 cm drop in coastal sea level associated with a 1 m s^{-1} increase in α_1 can be explained by geostrophic balance.

More interestingly, the correlations of α_2 with coastal sea level and wind stress were not statistically significant. We speculate that the second mode of variation is due primarily to changes in the local density field. *Smith and Schwing* [1991] have already shown that the mean vertical shear at mooring 3 can be explained in large part by the thermal wind relationship

$$\frac{\partial u}{\partial z} = \frac{g}{f\rho_0}\frac{\partial \rho}{\partial y} \tag{1}$$

where $\partial\rho/\partial y$ is the cross-shelf density gradient. The time variation in observed vertical shear at 70 m at mooring 3 is plotted in Figure 7, along with predictions based on (1). The observed and predicted shears are quite similar ($r^2 = 0.48$

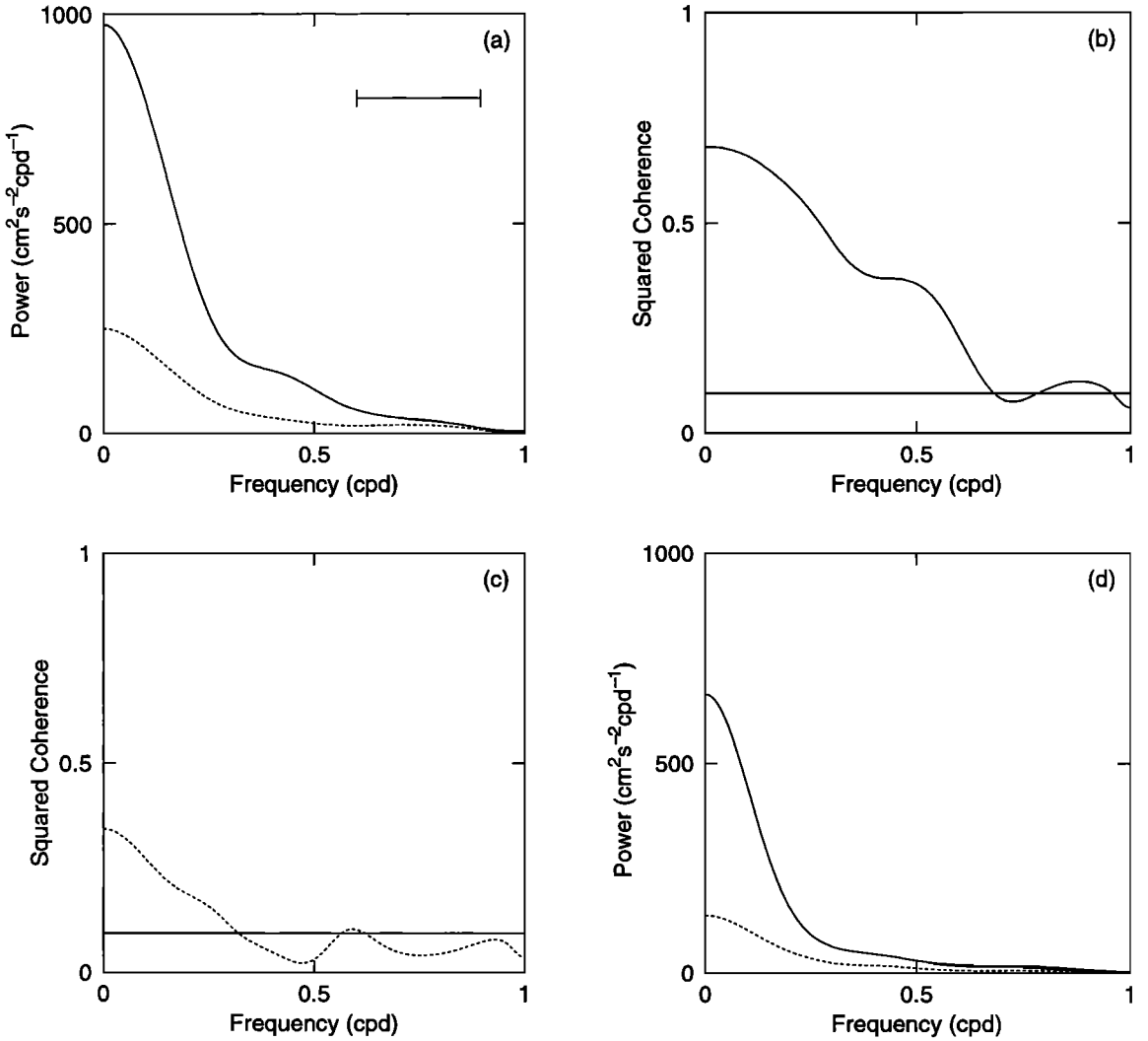

Figure 4. Spectral analysis of alongshore currents. (a) Power spectra for the meter at 25 m on mooring 1. The solid line is for the observed currents, and the dotted line is for residuals from the extended statistical model (see (21)). The horizontal bar shows the bandwidth. (b) Squared coherence between the observed alongshore currents at 25 m on mooring 1 and 23 m on mooring 2. The horizontal line is the 5% significance level for zero coherence. (c) As in Figure 4b, but for residuals from the extended statistical model. (d) As in Figure 4a, but for 23 m on mooring 2.

before smoothing), highlighting the importance of baroclinicity at this mooring.

To understand how α_2 can change without affecting coastal sea level, we will make some simplifying assumptions: The changes are so slow that the circulation at any time can be treated as steady (see lower panel of Figure 6a for justification); the circulation is not forced by the local wind (consistent with the low correlation between α_2 and the wind); the circulation does not vary significantly in the alongshore direction. The depth-integrated continuity equation and the coastal boundary condition of no-normal transport then imply that the cross-shelf transport is approximately zero everywhere. The depth-integrated, linearized momentum balance in the alongshore direction then implies that alongshore bottom stress must vanish because there is no other term to balance it. If bottom stress is parameterized in terms of bottom geostrophic velocity it follows that $\partial p/\partial y$ must vanish at the bottom. Following *Csanady* [1979], sea level at the coast relative to some offshore reference dynamic height is then given by

$$\Delta\eta = -\int_{-H}^{0} \epsilon_b \, dh \tag{2}$$

where h is the water depth, $\epsilon_b = (\rho_b - \rho_0)/\rho_0$ is the bottom density anomaly, and H is water depth at the offshore reference point. According to this expression, coastal sea level depends on the density along the bottom of the section but not on the density of the water above. Thus it is possible for the near-surface density field, and hence the position and width of a surface-intensified alongshore jet, to change without affecting coastal sea level.

In summary, the agreement between the observed and predicted vertical shears, the surface intensification of ϕ_2 at mooring 3 (Figure 6a), and the low correlation between α_2

Table 1. Statistics of Current Variability on the Halifax Line

Mooring (depth)	$s_u^2 + s_v^2$			$s_p^2/(s_u^2 + s_v^2)$			θ			γ^2	κ_o^2	κ_e^2
	1	2	3	1	2	3	1	2	3			
1(012)	235	112	156	0.87	0.81	0.79	23	19	17	0.66	0.52	0.28
1(025)	291	132	191	0.85	0.75	0.78	17	18	21	0.66	0.55	0.31
2(018)	132	52	71	0.87	0.76	0.74	8	11	12	0.54	0.61	0.27
2(023)	134	52	70	0.87	0.74	0.74	11	16	16	0.52	0.61	0.26
2(028)	116	46	59	0.87	0.74	0.74	16	21	22	0.51	0.60	0.22
2(030)	151	63	82	0.82	0.69	0.69	13	21	17	0.54	0.58	0.23
2(038)	115	50	60	0.87	0.76	0.74	7	15	15	0.52	0.57	0.17
3(016)	220	132	180	0.63	0.63	0.55	4	-21	-18	0.82	0.40	0.27
3(050)	171	121	148	0.74	0.74	0.67	-12	-20	-17	0.87	0.29	0.18
3(070)	168	106	136	0.73	0.70	0.64	-14	-21	-18	0.81	0.37	0.22
3(110)	125	53	86	0.80	0.63	0.67	-10	-15	1	0.69	0.58	0.38
4(070)	78	40	72	0.78	0.66	0.69	-22	-19	-23	0.92	0.49	0.44
4(110)	81	40	76	0.84	0.76	0.79	-36	-34	-39	0.94	0.51	0.47

Here s_u^2, s_v^2, and s_p^2 are variances (cm^2 s^{-2}) of currents in the alongshore, cross-shore, and major principal axis directions, respectively. The θ is the direction of the major principal axis (degrees, clockwise relative to 68°T). Column 1 refers to observations, column 2 to residuals from the statistical model (see (4)), and column 3 to hindcast errors from the circulation model. The γ^2 is the ratio of hindcast error variance to observed variance (column 3/column 1). The κ_o^2 is the proportion of observed variance accounted for by the statistical model (1−column 2/column 1). The κ_e^2 is the proportion of hindcast error variance accounted for by the statistical model (1−column 2/column 3).

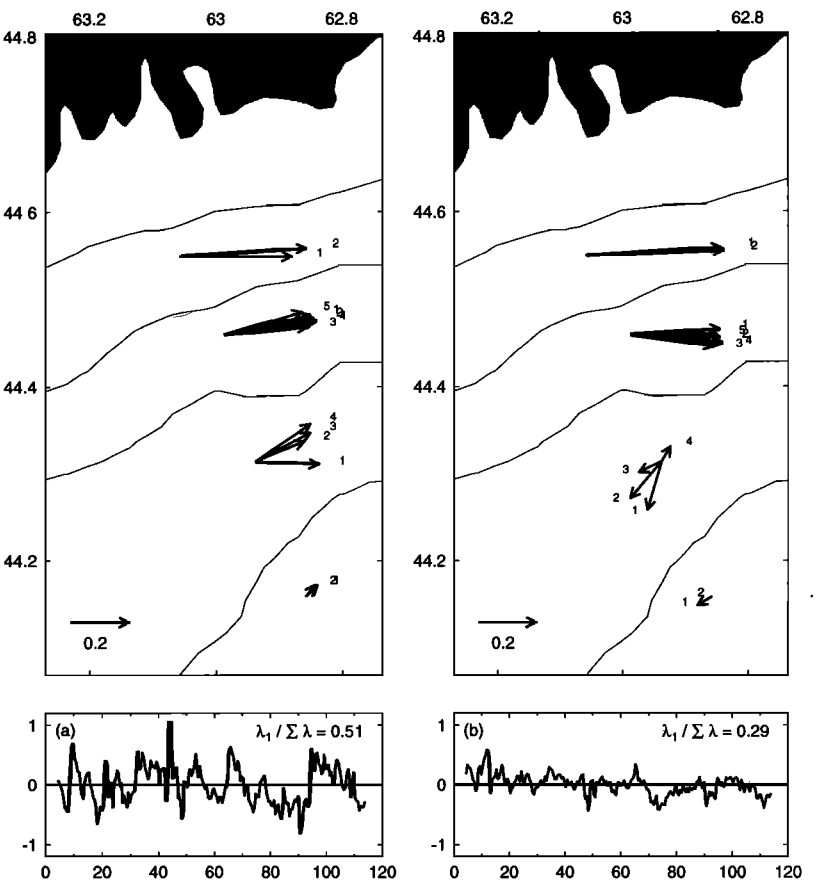

Figure 5. Principal component analysis of (a) observed currents and (b) residuals from the statistical model (see (4)). (Top) The eigenvector ($\vec{\phi}_1$) associated with the largest eigenvalue (λ_1) of the 26 × 26 uv covariance matrix. The numbers associated with each vector indicate the position of the current meter in the vertical. The smaller the number, the closer the meter to the sea surface (see Table 1). (Bottom) Variation in modal amplitude (α_1) in meters per second against time in days. The proportion of total current variance accounted for, $\lambda_1/\sum\lambda$, is given in the bottom panels.

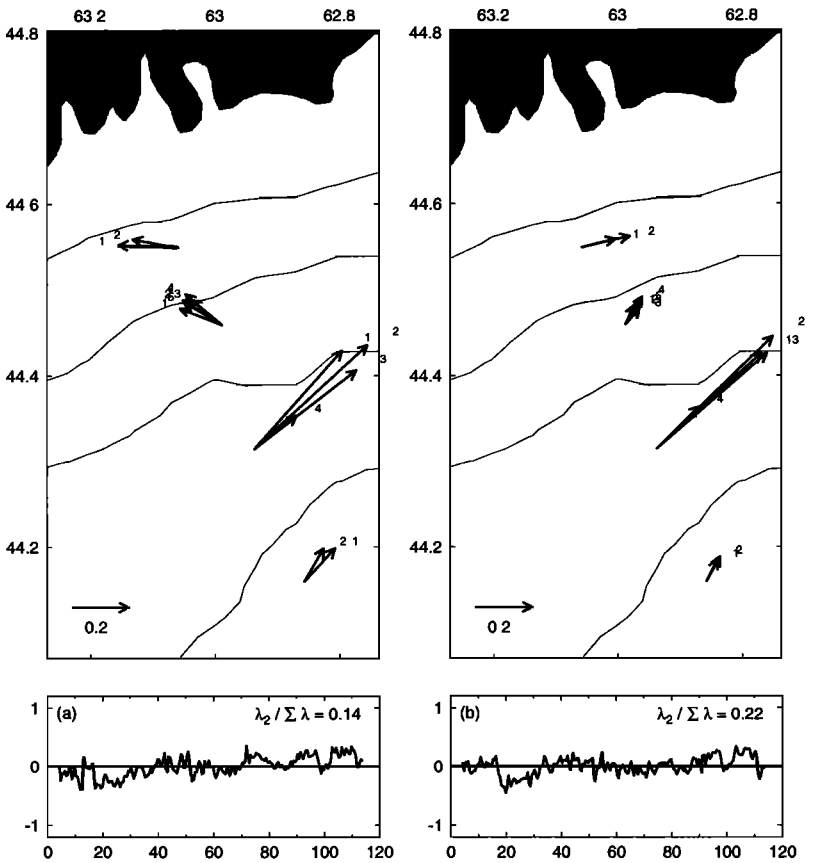

Figure 6. The ϕ and α for the second mode of variation. Otherwise, the same as Figure 5.

and coastal sea level lead us to speculate that the second mode of variation is due primarily to changes in the density field.

The orthogonality of the $\vec{\phi}_i$ makes their physical interpretation increasingly difficult as i increases. The modes for $i > 2$ individually account for less than 10% of the total variance and will not be discussed further.

To obtain an integral measure of the time-varying circulation, we calculated the transport through the Halifax Line from the 13 current meter records and the cross-sectional areas defined in Figure 2. In agreement with *Smith and Schwing* [1991] we found a mean transport to the southwest of $1.0 \times 10^6 \mathrm{m}^3\mathrm{s}^{-1}$ (Figure 8) for the CASP period. We also found variations that were strong enough to occasionally reverse the direction of the mean transport.

Residuals From the Statistical Model

Let u_t denote an observed current component at time t. We used a linear statistical model to decompose u_t into two parts:

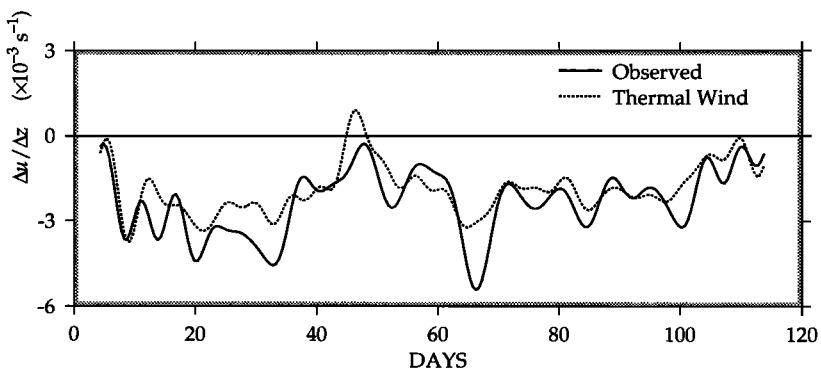

Figure 7. Vertical shear in the alongshore flow at 70 m depth, mooring 3. The solid line is the shear estimated from observed alongshore currents at 50, 70, and 110 m depth on mooring 3. The dotted line is the shear predicted from the thermal wind relationship using density measured at 70 m on moorings 2 and 4. See Figure 2 for the locations of the moorings and current meters. The time series were smoothed to pass only those motions with periods longer than 5 days.

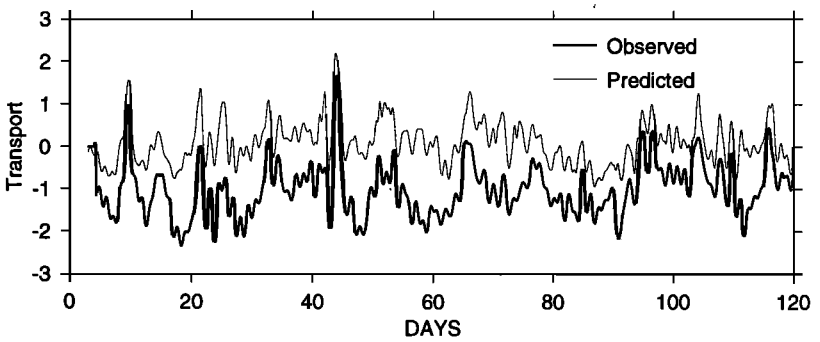

Figure 8. Transport through the Halifax Line. The observed transport (in units of $10^6 m^3 s^{-1}$) was calculated using the cross-sectional areas defined in Figure 2. The hindcasts were made with the circulation model driven with Sable wind stress and Louisbourg sea level. The mean of the hindcast transports has been removed.

$$u_t = u_t^s + e_t^s \tag{3}$$

where

$$u_t^s = \sum_j \left[a_j^s \eta_{t-j} + b_j^s \tau_{t-j}^x + c_j^s \tau_{t-j}^y\right] \tag{4}$$

is the part linearly related to Louisbourg sea level (η_t) and Sable wind stress (τ_t^x, τ_t^y) and e_t^s is a residual that is uncorrelated with these inputs at all lags (see the appendix). Superscript s denotes a quantity associated with the statistical model. The statistical model inputs are identical to those used to drive the circulation model.

The residual e_t^s is uncorrelated with u_t^s at zero lag, and so the variance of u_t partitions as follows:

$$\mathrm{Var}(u_t) = \mathrm{Var}(u_t^s) + \mathrm{Var}(e_t^s). \tag{5}$$

The ratio

$$\kappa_o^2 = \frac{\mathrm{Var}(u_t^s)}{\mathrm{Var}(u_t)} \tag{6}$$

is the proportion of current variance accounted for by the statistical model. It is also the maximum proportion of variance that can be accounted for by any linear, time-invariant model driven by Louisbourg sea level and Sable wind stress. Note that $0 \leq \kappa_o^2 \leq 1$.

The fit of the statistical model (see appendix for details) is best at mooring 2 and the deepest meter on mooring 3 (from Table 1, $0.57 \leq \kappa_o^2 \leq 0.61$). The fit is not quite as good at moorings 1 and 4 ($0.49 \leq \kappa_o^2 \leq 0.55$). The poorest fits are at the top 3 current meters on mooring 3 in the Nova Scotia Current ($0.29 \leq \kappa_o^2 \leq 0.40$). Averaging variances over the 13 current meters, we find that 50% of the observed current variance can be accounted for by the statistical model.

The coherence between moorings is reduced significantly by subtracting u_t^s from u_t. In other words, e_t^s has a smaller spatial scale than u_t. This is evident in the time series plots of u_t and e_t^s at the nearshore moorings (Figure 3) and their coherency spectra (compare Figure 4b and c). It is also reflected in the lower proportion of variance accounted for by the first mode of variation of e_t^s (29%, right panel of Figure 5) compared to u_t (51%, left panel of Figure 5). The first mode of residual variation may be interpreted as a depth-independent, coastal jet with the suggestion of a zero crossing between moorings 2 and 3 (Figure 5b). Its amplitude slowly drops by about 50 cm s^{-1} over the CASP period implying an increase in southwestward flow of about $0.5 \times 50 = 20$ cm s^{-1} at the nearshore moorings. The second mode of residual variation accounts for an additional 22% of the variance (Figure 6b). This mode and its amplitude are similar to the second mode of variation of the observations (compare Figure 6a and 6b). The physical origin of the residual modes is discussed in section 6 following an assessment of the hindcast skill of the circulation model.

3. Circulation Model

The continuity and horizontal momentum equations are taken to be

$$\frac{\partial \eta}{\partial t} + \nabla \cdot \int_{-h}^{0} \vec{u} dz = 0 \tag{7}$$

$$\frac{\partial \vec{u}}{\partial t} + \vec{f} \times \vec{u} = -g\nabla\eta + \frac{\partial}{\partial z}\left(\mu \frac{\partial \vec{u}}{\partial z}\right) \tag{8}$$

subject to the top and bottom boundary conditions (ST93)

$$\mu \frac{\partial \vec{u}}{\partial z} = \begin{cases} \vec{\tau}/\rho & z = 0 \\ k\vec{u} & z = -h. \end{cases} \tag{9}$$

Initial and lateral boundary conditions are defined later in this section.

Details of the numerical integration scheme are given by ST93. In essence, it involves subtraction of the steady Ekman flow ($\vec{u}_E$) from $\vec{u}$ before using the standard Galerkin spectral approach to solve for the remainder, $\vec{u}_R = \vec{u} - \vec{u}_E$. The remainder satisfies a pair of equations similar to (7) and (8) subject to (9) with $\vec{\tau} = 0$. To calculate $\vec{u}_R$, we expand it in terms of eddy viscosity eigenfunctions

$$\vec{u}_R = \sum_{s=1}^{M} \vec{U}_s(x, y, t)\psi_s(z) \tag{10}$$

where $\vec{U}_s$ is the amplitude of the sth eigenfunction ψ_s. The eigenfunctions satisfy the same boundary conditions as $\vec{u}_R$ and this accelerates the convergence of (10). The calculation of each $\vec{U}_s$ involves numerical integration of an equation similar to the depth-averaged momentum equation. The $\vec{U}_s$ equations are coupled by the continuity equation.

The governing equations for the $\vec{U}_s$ and η were discretized using a time step of 60 s and a grid spacing in x and y of 5.4 and 7.5 km, respectively. The bathymetry of the Scotian Shelf was kindly provided in digital form by D. Greenberg of the Bedford Institute of Oceanography. The model domain has one solid boundary and three open boundaries (Figure 1). The coastal boundary runs along the 10 m isobath, and the coastal boundary condition is no-normal transport. The offshore boundary coincides approximately with the 200 m isobath. For the case of a quiescent deep ocean, sea level is set to zero along the offshore boundary. The rationale for this boundary condition is that the continental slope insulates the shelf from the influence of low-frequency barotropic motions in the adjacent deep ocean [e.g., *Wang*, 1982]. We also carried out some sensitivity studies with sea level tilts imposed at the shelf break (section 4). The cross-shelf boundary conditions are more complicated. For the wind-forced cases we used the boundary condition proposed originally by *Orlanski* [1976] with the modification of *Miller and Thorpe* [1981]. Essentially, it is a forward-in-time, upstream differencing of the Sommerfeld radiation condition with the local phase speed estimated from interior values adjacent to the open boundaries. *Chapman* [1985] showed this boundary condition effectively damps seiching of the interior while retaining the correct low-frequency, wind-driven response. For remotely forced problems we prescribed sea level along the backward boundary and used the modified Orlanski condition at the forward boundary.

The initial condition was a state of rest. The spin-up time of the model is less than 2 days. Thus the initial condition is relatively unimportant for the integration times of interest here which exceed 100 days.

For k and μ we chose base values of 0.2 cm s^{-1} and 0.065 m^2 s^{-1}, respectively [e.g., *Heaps*, 1972]. This choice of μ corresponds to an Ekman depth of 36 m on the Scotian Shelf. We carried out some parameter sensitivity studies by varying k as described in section 6. The remaining parameters were taken to be $f = 1.022\times 10^{-4}s^{-1}$, $g = 9.81$ m s^{-2}, and $\rho_0 = 1025$ kg m^{-3}.

An important practical issue is the number of eigenfunctions, M, to use in (10). Clearly, this involves a trade-off between vertical resolution and computational efficiency. In a series of idealized numerical experiments, ST93 found that the differences in currents calculated with M equal to 4 and 50 were everywhere less than 0.5 cm s^{-1}. To test if such rapid convergence would hold with observed winds and realistic bathymetry, we set up two forms of the model, one with $M = 4$ and the other with $M = 50$ eigenfunctions. In both cases the model was forced by the observed values of Sable wind stress and Louisbourg sea level (see section 5). In accord with the idealized studies of ST93 we found the velocity differences were small, everywhere less than 0.5 cm s^{-1}. This is well below the generally accepted noise level of the current meters and much less than the standard deviation of the observed currents (Table 1). All of the flow fields described below were calculated with 4 eigenfunctions.

4. Steady Response of Model to Local and Remote Forcing

Aside from a weak nonlinearity associated with the modified Orlanski boundary condition the circulation model is linear. This means that its response to forcing by local wind and flows through open boundaries can be calculated and discussed separately. For all the steady state calculations described below we used a spin-up time of 25 days.

Local Wind

Wind forcing over the Scotian Shelf was assumed to be spatially uniform and equal to the mean stress calculated from winds observed at Sable Island during CASP. This corresponds to an eastward stress of 0.046 Pa which is close to the climatological winter mean for the region [*Drinkwater and Pettipas*, 1993]. Sea level along the backward and offshore boundaries was clamped at zero.

The sea level response is strongest at the coast (Figure 9a). At Halifax, for example, there is a mean setdown of 1.4 cm. This implies a gain of Halifax sea level on eastward wind stress of $-0.014/0.046 = -0.30$ m Pa^{-1}. In a statistical study of monthly mean sea level along the eastern seaboard of North America, *Thompson* [1986] regressed sea level on local wind stress and, for Halifax, found a gain for the eastward component of -0.32 ± 0.06 m Pa^{-1}. The good agreement between the two gains increases our confidence that the circulation model is correctly reproducing the overall response of the Scotian Shelf to forcing by local wind.

Most features in the depth-mean circulation pattern (Figure 9b) are straightforward to interpret. For example, the coastal jet is generally consistent with the arrested topographic wave theory of *Csanady* [1978]. The southward flow over Western and Sable Island Bank can be readily explained in terms of Ekman transport. Most of the flow onto the shelf required to balance the offshore Ekman transport is in the form of a topographically steered, geostrophic jet that runs along the shelf break and then shoreward through the deep saddle between Emerald and LaHave Bank.

Schwing [1992b] used a depth-averaged model to calculate the wind-driven circulation on the Scotian Shelf. Overall, his flow pattern is similar to the one presented in Figure 9b. The main differences are that we find more spatial variability on the eastern shelf and weaker flows over the banks on the western shelf. We suspect that the explanation is to be found in the smoothing applied to the bathymetry by Schwing (no smoothing was applied in the present study). The direction of the flow in the vicinity of Western Bank is also different: In the present study it is generally southward, whereas Schwing predicted a southeastward flow. The reason may be Schwing's parameterization of bottom stress in terms of depth-mean flow which causes the Ekman transport in shallow water to be more closely aligned with the wind.

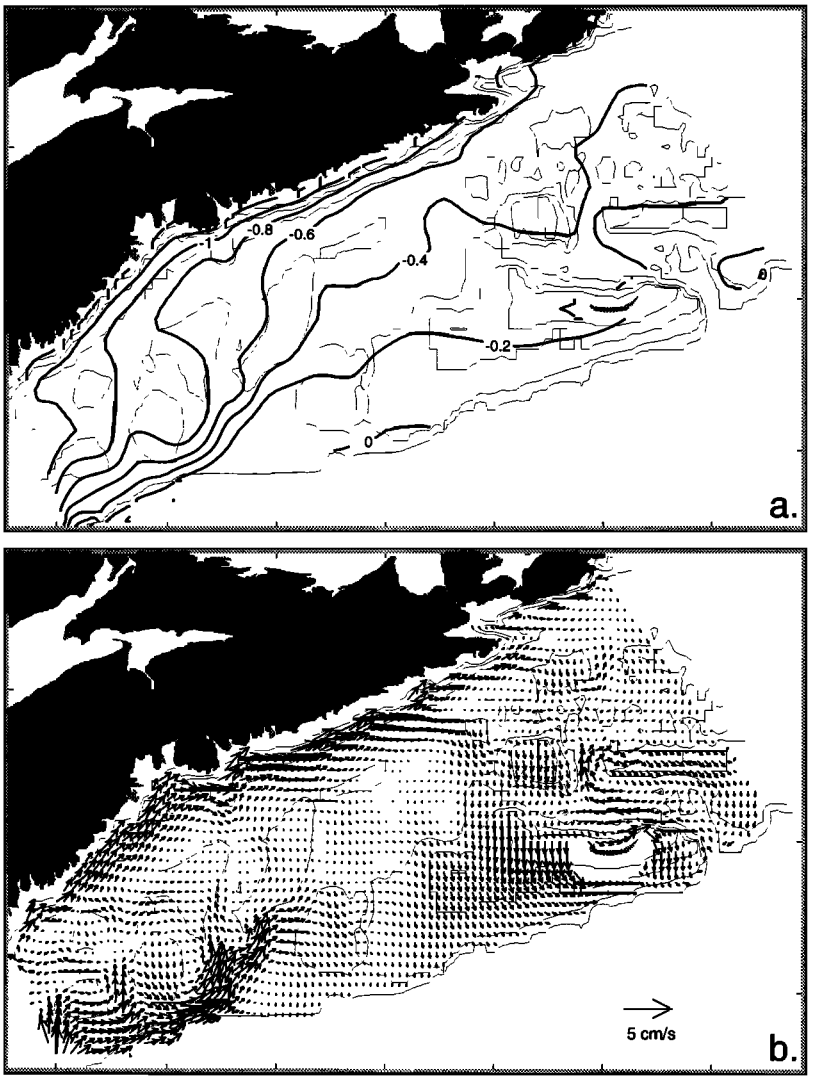

Figure 9. Response to the mean wind stress observed at Sable Island during CASP. (a) Sea surface elevation with a contour interval of 0.2 cm. (b) Depth-averaged currents. The thin lines are isobaths.

Surface currents (not shown) are more spatially uniform than the depth-mean flow, particularly over the outer shelf where they are generally consistent with surface Ekman drift. Inside the 100 m isobath the surface currents imply coastal upwelling. Bottom currents (not shown) are similar to the depth-mean currents over most of the shelf.

Backward Boundary

Sea level was assumed to drop linearly with distance along the backward boundary, from 20 cm at the coast to zero at the shelf break. Wind stress and sea level at the offshore boundary were both set to zero.

The model predicts a sea level drop of 8 cm along the coast of Nova Scotia (Figure 10a). Most of the drop takes place between the backward boundary and Halifax. The coastal boundary condition of zero normal transport means the alongshore tilt of coastal sea level must be balanced by bottom drag on the nearshore flow (Figure 10b).

In contrast to the wind-driven response, the circulation forced by the backward boundary is relatively weak over Western Bank and the inner part of the western shelf. As expected, the flow on the outer shelf is strongly steered by bathymetry. Most of the transport out of the model domain is between Emerald and LaHave Bank. Given that the surface boundary condition is zero vertical shear, it is not surprising that the surface and bottom currents (not shown) match closely the depth-mean flow over most of the shelf.

Deep Ocean

Sea level was assumed to drop linearly with distance along the offshore boundary, from 20 cm at the eastern end of the shelf to zero at the western end. Wind stress and sea level along the backward boundary were both set to zero.

The model predicts a coastal sea level drop of 4 cm from east to west, about half of the response forced by the backward boundary (Figure 11a). One implication of this smaller sea level drop is that, for a given head, the deep ocean is not as effective as the backward boundary at driving nearshore circulation (compare Figures 10 and 11).

According to the model, the exchange between the shelf and deep ocean takes place mainly in The Gully, just to the east of Sable Island. There is also a broad onshore flow over

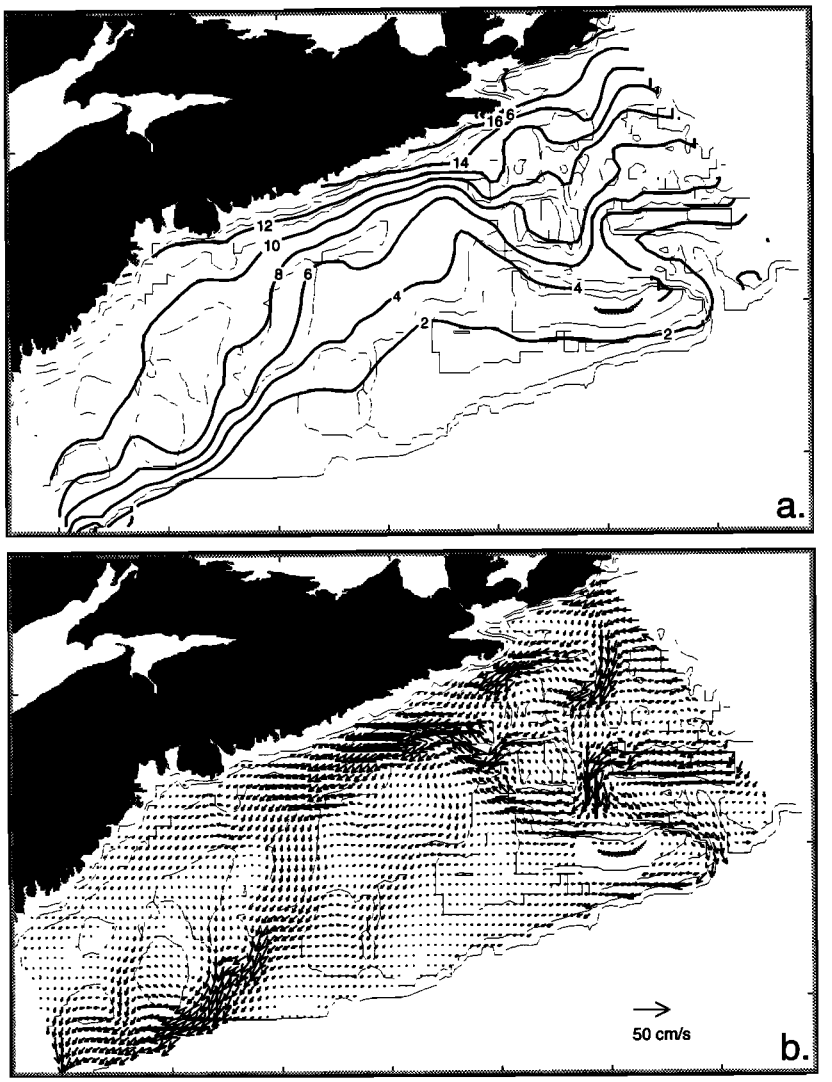

Figure 10. Response to a steady sea level setup along the backward boundary. Sea level decreases linearly from 20 cm at the coast to zero at the shelf break. (a) Sea surface elevation with a contour interval of 2 cm. (b) Depth-averaged currents. The thin lines are isobaths.

the flank of Western Bank (Figure 11b). The circulation over the central and western shelf is similar to that forced by flow through the backward boundary (compare Figures 10b and 11b).

5. Hindcasting CASP Circulation

For the next set of numerical integrations the wind was allowed to change with time. It was, however, assumed spatially uniform and equal to that observed at Sable Island (Figure 3). The backward boundary condition was specified by requiring that sea level vary linearly with distance from shore, ranging from the observed value at Louisbourg to zero at the shelf break (Figure 3). Two typical time series of hindcast currents at the nearshore moorings are plotted in Figure 3.

Methodology

To assess the skill of the circulation model, we use the same approach used to assess the fit of the statistical model (4). Let u_t denote an observation. Then

$$u_t = u_t^c + e_t^c \tag{11}$$

where u_t^c is the circulation model hindcast and e_t^c is the hindcast error. (Superscript c is used to denote quantities associated with the circulation model.) In general, u_t^c and e_t^c will be correlated, and it is not possible to define a κ^2 for the circulation model in the same way as the statistical model. However, it is still possible to form the ratio of hindcast error variance to observed variance:

$$\gamma^2 = \frac{\mathrm{Var}(e_t^c)}{\mathrm{Var}(u_t)} \tag{12}$$

We use γ^2 to measure the hindcast skill of the circulation model. Clearly, the smaller the γ^2, the better the hindcast. If γ^2 exceeds unity, the observed variance increases with the subtraction of the hindcasts from the observations. Note that γ^2 greater than or equal to unity does not imply that the observations and hindcasts are uncorrelated. For example, if γ^2 equals unity, the correlation between u_t and u_t^c is

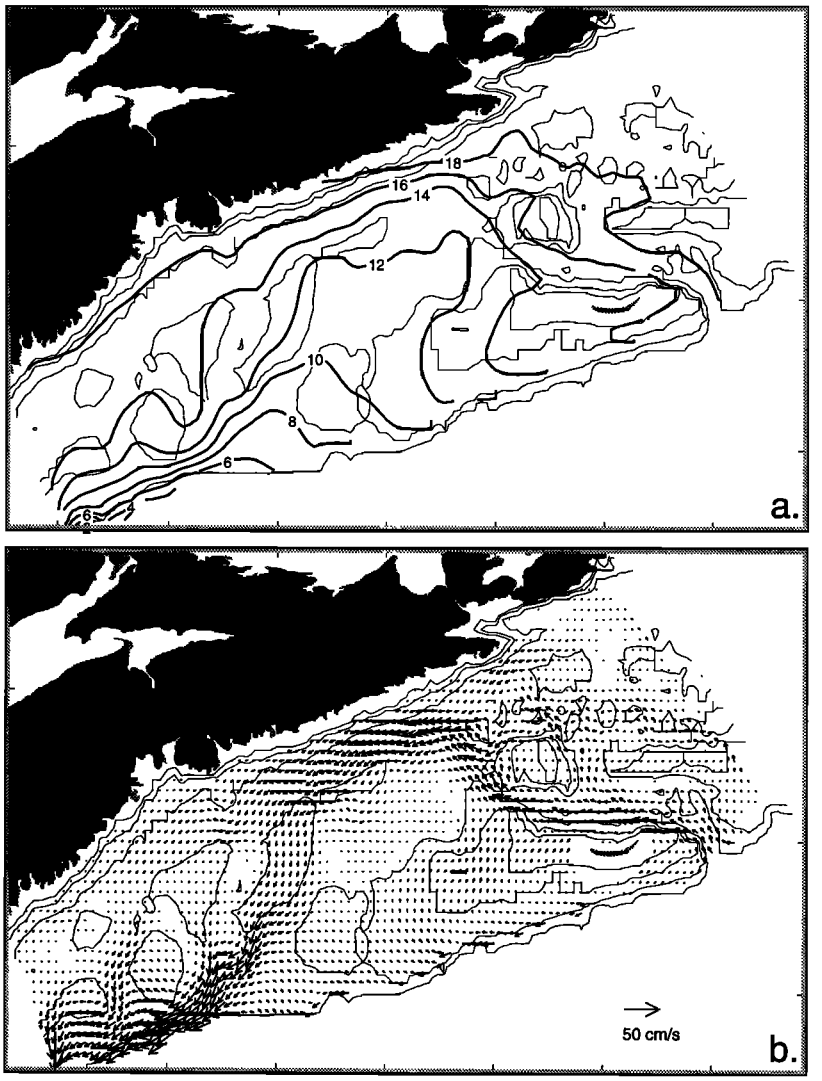

Figure 11. Response to a steady sea level setup along the offshore boundary. Sea level decreases approximately linearly with distance along the offshore boundary, from 20 cm at the eastern end of the shelf to zero at the western end. (a) Sea surface elevation with a contour interval of 2 cm. (b) Depth-averaged currents. The thin lines are isobaths.

$$\mathrm{corr}(u_t, u_t^c) = \frac{1}{2}\sqrt{\frac{\mathrm{Var}(u_t^c)}{\mathrm{Var}(u_t)}} \tag{13}$$

One possible reason for low model skill or, equivalently, a high γ^2 is that the observations are dominated by measurement noise. Another possibility is that the dynamical model is deficient in some important way. To help interpret γ^2, we split the hindcast error into a component due to the suboptimality of the circulation model ($u_t^s - u_t^c$) and a component that is uncorrelated with the model inputs at all lags (e_t^s):

$$e_t^c = u_t^s - u_t^c + e_t^s \tag{14}$$

If the circulation model is linear and the effect of initial conditions on the hindcasts is ignored (in practice this means short spin-up times and long integrations), then u_t^c can be expressed in a form that parallels (4):

$$u_t^c = \sum_j \left[a_j^c \eta_{t-j} + b_j^c \tau_{t-j}^x + c_j^c \tau_{t-j}^y\right] \tag{15}$$

The weights in this equation are time invariant. They depend on the parameters in the governing equations, the boundary conditions, and the discretization. Given e_t^s is uncorrelated with the model inputs at all lags, e_t^s is uncorrelated with u_t^c. Thus the variance of the hindcast error can be partitioned in a way that parallels (5):

$$\mathrm{Var}(e_t^c) = \mathrm{Var}(u_t^s - u_t^c) + \mathrm{Var}(e_t^s) \tag{16}$$

Following the definition of κ_o^2 given by (6), we can then define

$$\kappa_e^2 = \frac{\mathrm{Var}(u_t^s - u_t^c)}{\mathrm{Var}(e_t^c)} \tag{17}$$

This is the proportion of hindcast error variance that can be attributed to the suboptimality of the circulation model. It is also the most one can expect to reduce the variance of the hindcast errors by, for example, tuning model parameters or adjusting the form of the open boundary conditions. If the estimated value of κ_e^2 is not significantly different from

zero (see appendix), the skill of the circulation model can be considered effectively optimal.

With the above definitions of κ_o^2 and κ_e^2 it follows that

$$\gamma^2 = \frac{1-\kappa_o^2}{1-\kappa_e^2} \tag{18}$$

If the circulation model is optimal ($u_t^c = u_t^s$), then $\kappa_e^2 = 0$ and γ^2 achieves its minimum value of

$$\gamma_{\min}^2 = 1 - \kappa_o^2 \tag{19}$$

On the other hand, if the hindcast errors remain highly coherent with Louisbourg sea level and Sable wind stress, then κ_e^2 will be close to unity and γ^2 will greatly exceed $\gamma_{\min}^2$.

Results

The skill of the circulation model is highest at mooring 2 ($\gamma^2 = 0.5$, Table 1). At two of the meters on this mooring (28 and 38 m), κ_e^2 is not significantly different from zero, implying that the hindcast skill of the circulation and statistical models are effectively equal ($\gamma_{\min}^2 = 1 - \kappa_o^2 = 0.4$). At the other 3 meters on this mooring the suboptimality of hindcasts is not of great practical significance. At the top meter for example, the standard deviation of flow along the principal axis of variation is 7.3 cm s^{-1} for e_t^c and 6.2 cm s^{-1} for e_t^s.

Currents are less coherent with Louisbourg sea level and Sable wind stress at mooring 1 ($\kappa_o^2 = 0.5$ compared to $\kappa_o^2 = 0.6$ for mooring 2). Thus one would expect the circulation model to have lower skill at this mooring. In fact, we find $\gamma^2 = 0.7$. We also find that a statistically significant proportion of hindcast error variance can be accounted for by motions that remain coherent with the model inputs ($\kappa_e^2 = 0.3$). This leads us to conclude that the skill of the circulation model can be increased slightly at mooring 1.

We found that κ_e^2 is not significantly different from zero at the meters at 50 and 70 m on mooring 3 ($\kappa_e^2 = 0.2$). Thus, even though the hindcasts are not particularly impressive ($\gamma^2 = 0.87, 0.81$), they are close to optimal. The performance of the circulation model at the deepest meter on mooring 3 is similar to that at mooring 1 ($\gamma^2 = 0.7$, $\kappa_e^2 = 0.4$).

The hindcast skill of the circulation model is lowest at mooring 4 ($\gamma^2 = 0.9$). Both κ_o^2 and κ_e^2 are about 0.5, and so neither the circulation model nor the statistical model fit the observations particularly well. The high values of κ_e^2 suggest that it should be possible to improve significantly the hindcasts of the circulation model at this mooring.

There is good agreement between the variations in observed and hindcast transport through the Halifax Line (Figure 8). Treating observed transport as the dependent variable in (11), we find $\gamma^2 = 0.40$. To interpret this ratio, we note that $\kappa_e^2 = 0.34$, a value that is significantly different from zero. This suggests there is room for model improvement. However, we note that the standard deviation of the errors of the circulation and statistical model are 0.39 and 0.32×10^6 m^3 s^{-1} respectively. By way of contrast the standard deviation of the observed transport is 0.62×10^6 m^3 s^{-1}. Thus, for practical purposes we consider the circulation model to be effectively optimal with regard to transport.

One reason for the difference in the mean of the observed and predicted transport (Figure 8) is that we do not know the exact datum of the sea level used to specify the backward boundary condition. We specified the datum by equating the mean sea level at Louisbourg to the mean level of the adjacent deep ocean. The hindcast transport plotted in Figure 8 has zero mean. Another reason to expect a difference in the means is that the observed transport has a significant baroclinic component [*Smith and Schwing*, 1991] that is not captured by our barotropic model.

6. Improving the Hindcasts

Using (4), (14), and (15) it is possible to express the hindcast error of the circulation model in the following form:

$$e_t^c = \sum_j \left[\tilde{a}_j \eta_{t-j} + \tilde{b}_j \tau_{t-j}^x + \tilde{c}_j \tau_{t-j}^y\right] + e_t^s \tag{20}$$

where $\tilde{a}_j = a_j^s - a_j^c$ and, similarly, for $\tilde{b}_j$ and $\tilde{c}_j$. These sequences of weights define the differences in the response of the statistical and circulation model to forcing by Louisbourg sea level and Sable wind stress.

Fourier transforms of the $\tilde{a}_j$ sequences suggest that the circulation model underestimates the low–frequency (< 0.1 cpd) response at mooring 1 to backward boundary forcing and overestimates the response at mooring 4. We considered the possibility that our choice of bottom friction coefficient was too high. With a smaller k (see (9)) one would expect a narrower frictional boundary layer adjacent to the coast. This in turn should strengthen the flow at the nearshore moorings and weaken it at the offshore mooring. Reducing k to 0.1 cm s^{-1} did indeed intensify the coastal jet at lower frequencies as expected. However, it did not explain the suboptimal skill of the circulation model. Although the hindcast error variance decreased at mooring 4 (γ^2 dropped from 0.94 to 0.68 at the deepest meter), γ^2 increased at the other moorings.

Another explanation for the underestimation of nearshore currents may be that our assumption of a linear sea level profile along the backward boundary is not valid at all frequencies. Although a linear profile may be reasonable for first-mode shelf waves propagating through the region with periods of several days, it may not be realistic at lower frequencies. It is possible, for example, that the low-frequency flow through the backward boundary is dominated by outflows from the Gulf of St. Lawrence that are trapped close to shore by bathymetry. The assumption of a linear drop of sea level across the backward boundary would result in a coastal boundary current that is too wide at low-frequency. This would lead to underestimation of the nearshore flow and overestimation in deeper water consistent with the Fourier transforms of the $\tilde{a}_j$ sequences.

The $\tilde{b}_j$ and $\tilde{c}_j$ sequences and their Fourier transforms define the differences in the response of the circulation and statistical models to forcing by the wind. Overall, they had more spatial structure and frequency dependence than the $\tilde{a}_j$ sequences and their transforms and were generally more difficult to interpret.

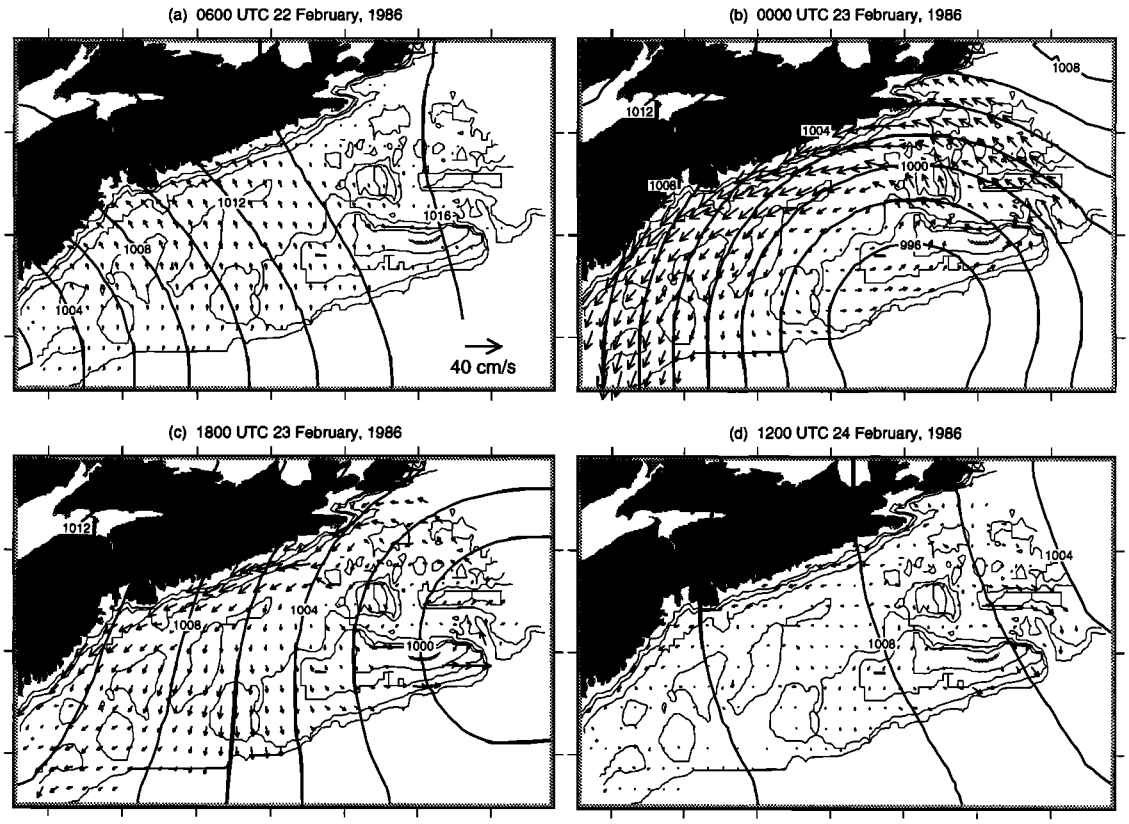

Figure 12. Circulation driven by spatially variable winds. The contour lines show the air pressure distribution. The vectors are the hindcast surface currents shown every third grid point. Time increases from left to right, top to bottom. The time between consecutive panels is 18 hours.

One reason for the nonzero $\tilde{b}_j$ and $\tilde{c}_j$ may be our use of a spatially uniform wind field. During the passage of intense storms, the wind field over the Scotian Shelf can have significant spatial structure (Figure 12). If winds at different locations on the Scotian Shelf are coherent with observations at Sable Island, the statistical model will capture the full wind effect. The circulation model, on the other hand, will be driven by the wrong wind field, and this will increase both the hindcast error variance and γ^2.

To quantify the effect of spatial structure in the wind field, we transformed some of the surface analysis maps presented by *Strapp et al.* [1988] into maps of wind stress (Figure 12). This involved the calculation of gradient winds for all model grid points, a scaling and rotation to best fit Sable Island observed wind, and finally a transformation into stress. Figure 13 shows the improvement in the hindcasts of transport that can result from allowing for spatial structure in the wind during the passage of intense storms. Note that the surface

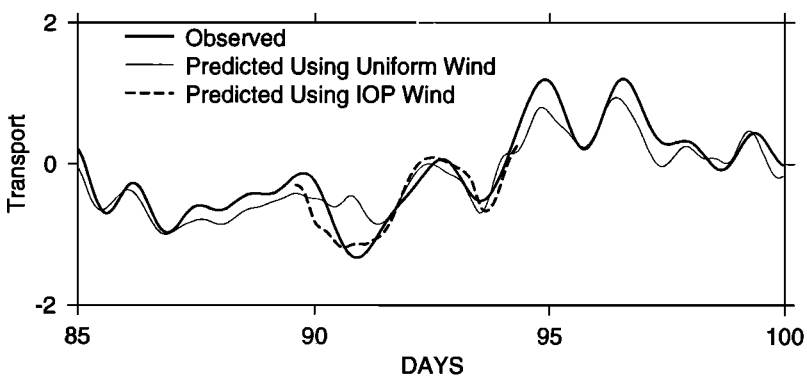

Figure 13. Observed and hindcast transport (10^6 m^3 s^{-1}) through the Halifax Line during one CASP intense observation period. The "uniform wind" hindcasts were calculated by the model forced by Sable wind stress and Louisbourg sea level. The "IOP wind" hindcasts were calculated using spatially variable winds and Louisbourg sea level. The means have been removed.

currents (Figure 12) are roughly parallel to the local wind on the outer shelf, again highlighting the importance of spatial variations in the wind.

A different type of contribution to the hindcast error comes from motions that are incoherent with Louisbourg sea level and Sable wind stress (e_t^s in (20)). To explore the physical origin of this contribution, we added physically meaningful variables to the statistical model (4) and checked if the reduction in residual variance (equivalently the increase in κ_o^2) was statistically significant.

Adding the thermal wind index to the statistical model gave significant improvements in skill at the top 3 current meters on mooring 3: the proportion of variance accounted for by the statistical model increased from $0.29 \leq \kappa_o^2 \leq 0.40$ to $0.49 \leq \kappa_o^2 \leq 0.56$. This is in accord with our earlier conclusion that baroclinicity is important at this mooring (section 2). A smaller but statistically significant reduction in variance was achieved at the two near-surface meters on mooring 1.

Alongshore wind stress from Yarmouth was added to the statistical model in an attempt to allow for spatial structure in the wind field. Significant improvements in fit were found at the two nearshore moorings and the deepest current meter on mooring 3. The biggest improvement was at mooring 1 where κ_o^2 increased by almost 0.1. We conclude that variations in the wind field that are incoherent with Sable Island wind can have a significant effect on the circulation.

In a recent modeling study of the time-varying circulation on the Labrador and Newfoundland shelf, *deYoung et al.* [1995] concluded that air pressure can have an important effect on bottom pressure, and hence on the circulation, on timescales of 4 to 10 days. In a series of sensitivity studies they confirmed the hypothesis of *Wright et al.* [1987] that air pressure over Hudson Bay can generate measurable currents on the Labrador Shelf. To test if air pressure over the Scotian Shelf and Gulf of St. Lawrence can drive measurable currents on the Scotian Shelf, we added local air pressure to (4). The drop in residual variance was not significantly different from zero leading us to conclude the effect of air pressure on the circulation can be ignored in this region.

Coastal sea level is straightforward to measure and, as demonstrated by the hindcast skill of the circulation model at the nearshore moorings, can provide useful information on the circulation of the coastal ocean. Can the performance of the statistical model be improved significantly by adding more coastal sea levels? We tried adding various coastal bottom pressures and sea levels (see Figure 1) to (4) and found that overall, Whitehead Harbour was the most effective at reducing the residual variance. Although the improvement in fit was statistically significant at the two nearshore moorings (κ_o^2 increased by about 0.05), it was not of much practical significance.

To conclude this section, we fit the following extended form of the statistical model to the currents

$$u_t^s = u_t^s(\eta, \tau^x, \tau^y, \partial\rho/\partial z, \tau_Y^y, \eta_W) \qquad (21)$$

where η and (τ^x, τ^y) are Louisbourg sea level and Sable wind stress as before, $\partial\rho/\partial z$ is the thermal wind index, τ_Y^x is alongshore wind stress at Yarmouth, and η_W is Whitehead Harbour sea level. (In this notation the original statistical model is $u_t^s(\eta, \tau^x, \tau^y)$). Averaging variances across all current meters, we find that 67% of the observed current variance can be accounted for by the extended statistical model compared to 50% for the original model. The individual κ_o^2 for the extended model all lie between 0.55 and 0.75. Figure 4a and 4d illustrate the reduction in variance associated with the removal of (21) from the observations, and Figure 4b and 4c illustrate the reduction in coherence between the nearshore moorings. Another way of illustrating the reduced spatial scale of the residuals from the extended statistical model is with the proportion of total variance accounted for by their first mode of variation: It is 22% compared to 29% for the residuals from the original model (4). What remains after removal of $u_t^s(\eta, \tau^x, \tau^y, \partial\rho/\partial z, \tau_Y^y, \eta_W)$ from u_t are essentially localized current variations with a spatial scale that is of the order of the minimum separation between the moorings.

7. Discussion

We were encouraged to find that a linear, barotropic model forced by local wind stress and coastal sea level could provide relatively good hindcasts of the along-shelf transport variations observed during CASP. Specifically, the hindcast error variance was 40% that of the observed transport variance (γ^2=0.4). Comparison of these hindcasts against those of a statistical model led us to conclude that the circulation model is effectively optimal with respect to transport. The skill of the circulation model is more variable with respect to currents. It is effectively optimal about 30 km from shore ($\gamma^2 \approx 0.5$) and least effective and definitely suboptimal, 65 km from shore ($\gamma^2 \approx 0.9$).

We gave two reasons for the difference in the skill of the circulation and statistical model. The most straightforward reason is that we did not allow for spatial structure in the wind field. The most direct evidence for this came from running the circulation model with spatially variable wind fields that we estimated for one CASP intense observation period. The result was a noticeable improvement in model skill. Indirect evidence came from the significant improvement in the fit of the statistical model with the addition of more wind stress terms. Allowing for spatial variations in future studies should be straightforward because gridded nowcasts and forecasts of the wind field with a resolution of about 30 km are made routinely for this region by the Atmospheric Environment Service of Canada. The other reason for the suboptimal performance of the circulation model may be the form of the backward boundary condition. Based on the different responses of the circulation and statistical models to periodic variations in Louisbourg sea level we speculate that the form of the backward boundary condition should be allowed to vary with frequency, with longer period inflows trapped closer to shore. This modification should be straightforward to implement.

Adding thermal shear $\partial\rho/\partial y$ to the statistical model led to significant improvements in fit at the mooring located in the

Nova Scotia Current. Allowing for baroclinicity in an operational circulation model will be difficult. The variations in shear are probably due to seasonal variations in the circulation associated with outflow from the Gulf of St. Lawrence and instability of the Nova Scotia Current (see *Petrie, et al.* [1987] for a discussion of barotropic-baroclinic instability in this region). Given that $\partial\rho/\partial y$ is essentially uncorrelated with the local wind and coastal sea level, the inclusion of baroclinicity in an operational model of the region will probably require the assimilation of more data, including currents and densities from fixed moorings and sea-surface temperature distributions from satellites.

It is straightforward to force circulation patterns in the model that have no signature in coastal sea level. To illustrate, assume sea level along the backward boundary varies linearly from zero at the coast to 20 cm at the shelf break and then linearly along the shelf break to zero at the forward boundary. The resulting flow pattern (the difference of Figures 11b and 10b) has a coastal jet with no signature in Louisbourg sea level. However, this circulation pattern does have a signature in differences in coastal sea level because an alongshore head is required to drive the coastal jet against bottom friction. This raises the possibility that an array of coastal sea level stations may be more effective in estimating the backward boundary condition than Louisbourg sea level alone. We tested this idea by adding more coastal sea levels to the statistical model. Although statistically significant reductions in residual variance were achieved, the improvement in fit was not of great practical significance on the Halifax Line.

In summary we have demonstrated that our linear, barotropic circulation model of the Scotian Shelf has significant hindcast skill in the meteorological band. Significant improvements in skill will be achieved by allowing for spatial structure in the wind field, a frequency-dependent relationship between coastal sea level and the backward boundary condition and, most importantly, the evolution of the density field with the flow.

Appendix

Calculating Residuals From the Statistical Model

To estimate the residuals e_t^s, we first Fourier transform (3) and (4) and estimate the frequency-dependent transfer functions $A(\omega) = \sum_j a_j e^{i\omega j}$, and similarly $B(\omega)$ and $C(\omega)$, from the power and cross spectra of u_t, η_t, τ_t^x, and τ_t^y [*Priestley*, 1981, section 9.3]. These transfer functions are then used to correct the Fourier transform of u_t for the effect of wind and sea level. The residual time series is then found by inverse Fourier transform.

The main difficulty with the implementation of this approach is deciding on the amount of smoothing to apply to the power and cross-spectral estimators, that is, choosing the bandwidth. We tackled this problem in two ways. First, we applied the technique of "window closing" as described by *Jenkins and Watts* [1968]. We found a bandwidth of 0.0868 cpd produced reasonable results. Typical power and coherency spectra estimated with this bandwidth are shown in Figure 4. Second, we fit (4) in the time domain, with j taking on a successively larger range of values, and plotted Akaike's Information Criterion (AIC) against the number of adjustable parameters in the model [*Akaike*, 1974]. The AIC is proportional to $n \log s_e^2 + 2q$, where n is the number of independent observations to which the model is fit, q is the number of adjustable parameters, and s_e^2 is the residual variance [*Priestley*, 1981, section 5.4]. The minimum AIC was achieved with 12 hour sea levels and wind stresses lagged by less than about 3 days. (We restricted the class of models to those that were physically realizable, i.e., $j > 0$). Both time domain and frequency domain approaches gave very similar residual time series.

We also fit (4) to the currents hindcast by the circulation model (i.e., we took u_t^c as the dependent variable instead of u_t). Given that the circulation and statistical model are forced by the same inputs (Louisbourg sea level and Sable wind stress), we would hope for a perfect fit. Using a bandwidth of 0.0868 cpd, we found the statistical model accounted for 99% of the hindcast variance (i.e., $\gamma^2 = 0.01$). This demonstrates that the frequency-dependent response of the circulation model to forcing by wind and sea level is adequately resolved by the statistical model.

Significance of κ^2

To test if the estimates of κ_o^2 or κ_e^2 are significantly different from zero, we used the following Monte-Carlo procedure:

1. Calculate the Fourier transform of the input series (u_t for κ_o^2 and e_t^c for κ_e^2).
2. Randomize the phases of this transform and invert to obtain a new realization with the same serial dependence as the input series.
3. Fit the statistical model (4) to the new realization as outlined in the preceding section.
4. Estimate and record κ^2.

Repeat these steps many times and estimate the distribution of κ^2 under the null hypothesis that its true value is zero. The estimated values of κ_o^2 or κ_e^2 were then tested to see if they were statistically different from zero at any given level of significance. In this study we used 5%.

Acknowledgments. We first thank our colleagues at the Bedford Institute of Oceanography, for their support and generous provision of data, and Maureen Cribb for her help in estimating wind fields. We also thank the anonymous reviewers for their comments. The work was funded by the Natural Sciences and Engineering Research Council of Canada, through the Ocean Production Enhancement Network and the follow-on Interim Funding Research Programme, and by IBM through their Environmental Research Program.

References

Akaike, H., A new look at the statistical model identification, *IEEE Trans. Autom. Control, AC-19, 6*, 716-723, 1974.

Anderson, C., and P. C. Smith, Oceanographic observations on the Scotian Shelf during CASP, *Atmos. Ocean, 27*, 130-156, 1989.

Chapman, D. C., Numerical treatment of cross-shelf open boundaries in a barotropic coastal ocean model, *J. Phys. Oceanogr., 15*, 1060-1075, 1985.

Csanady, G. T., The arrested topographic wave, *J. Phys. Oceanogr., 8*, 47-62, 1978.

Csanady, G. T., The pressure field along the western margin of the North Atlantic, *J. Geophys. Res., 84*, 4905-4915, 1979.

DeYoung, B., Youyu Lu, and R. Greatbatch, Synoptic bottom pressure variability on the Labrador and Newfoundland continental shelves, *J. Geophys. Res., 100*, 8639-8653, 1995.

Drinkwater, K. F., and E. G. Pettipas, Climate data for the northwest Atlantic: Surface wind stresses off eastern Canada, 1946-1991, *Can. Data Rep. of Hydrogr. and Ocean Sci., 123*, 130 pp., Dep. of Fish. and Oceans, Halifax, N.S., 1993.

Heaps, N. S., On the numerical solution of the three-dimensional hydrodynamical equations for tides and storm surges, *Mem. Soc. R. Sci. Liege, 6*(1), 143-180, 1972.

Jenkins, G. M., and D. G. Watts, *Spectral Analysis and its Applications*, 525 pp., Holden-Day, Merrifield, Va., 1968.

Large, W. G., and S. Pond, Open ocean momentum flux measurements in moderate to strong winds, *J. Phys. Oceanogr., 11*, 324-336, 1981.

LeBlond, P. H., and L. A. Mysak, *Waves in the Ocean, Oceanogr. Ser.* Vol. 20, 602 pp., Elsevier, New York, 1978.

Lively, R. R., Current meter, meteorological, sea-level and hydrographic observations from the CASP experiment, off the coast of Nova Scotia, November 1985 to April 1986, in *Can. Tech. Rep. Hydrogr. and Ocean Sci., 100*, 428 pp., Dep. of Fish. and Oceans, Halifax, N.S., 1988.

Miller, M. J., and A. J. Thorpe, Radiation conditions for the lateral boundaries of limited-area numerical models, *Q. J. R. Meteorol. Soc., 107*, 615-628, 1981.

Orlanski, I., A simple boundary condition for unbounded hyperbolic flows, *J. Comput. Phys., 21*, 251-269, 1976.

Petrie, B., B. J. Topliss, and D. G. Wright, Coastal upwelling and eddy development off Nova Scotia, *J. Geophys. Res., 92*, 12,979-12,991, 1987.

Priestley, M. B., *Spectral Analysis and Time Series*, 890 pp., Academic, San Diego, Calif., 1981.

Schwing, F. B., Subtidal response of the Scotian Shelf bottom pressure field to meteorological forcing, *Atmos. Ocean, 27*, 157-180, 1989.

Schwing, F. B., Subtidal response of Scotian Shelf circulation to local and remote forcing, I, Observations, *J. Phys. Oceanogr., 22*, 523-541, 1992a.

Schwing, F.B., Subtidal response of Scotian Shelf circulation to local and remote forcing, II, Barotropic model, *J. Phys. Oceanogr., 22*, 542-563, 1992b.

Sheng, J., and K. R. Thompson, A modified Galerkin-spectral model for three-dimensional, barotropic, wind-driven shelf circulation, *J. Geophys. Res., 98*, 7011-7022, 1993.

Smith, P. C., and F. B. Schwing, Mean circulation and variability on the eastern Canadian continental shelf, *Cont. Shelf Res., 11*, 977-1012, 1991.

Strapp, J. W., J. Power, and K. Macdonald, CASP field summary, *Atmos. Environ. Serv., Environ. Can.*, 1988.

Thompson, K. R., North Atlantic sea level and circulation, *Geophys. J. R. Astron. Soc., 87*, 15-32, 1986.

Wang, D-P., Effects of continental slope on the mean shelf circulation, *J. Phys. Oceanogr., 12*, 1524-1526, 1982.

Wright, D. G., D. A. Greenberg, J. W. Loder, and P. C. Smith, The steady-state barotropic response of the Gulf of Maine and adjacent regions to surface wind stress, *J. Phys. Oceanogr., 16*, 947-966, 1986.

Wright, D. G., D. A. Greenberg, and F. G. Majaess, The influence of bays on adjusted sea level over adjacent shelves with application to the Labrador Shelf, *J. Geophys. Res., 92*, 14,610-14,620, 1987.

K. R. Thompson and J. Sheng, Department of Oceanography, Dalhousie University, Halifax, Nova Scotia, Canada, B3H 4J1. (e-mail: Keith.Thompson@Dal.Ca; Jinyu.Sheng@Dal.Ca)

(Received August 29, 1994; revised March 28, 1996; accepted April 16, 1996.)